

Antennifying Orthopedic Bone-Plate Fixtures for the Wireless Monitoring of Local Deep Infections

P. Avaltroni, S. Nappi, *IEEE Student Member* and G. Marrocco, *IEEE Senior Member*

Abstract—Infection is the unavoidable threat to any orthopedic implant that can also force its removal as extreme remedy. The diagnosis of infections is currently achieved by time consuming imaging (X-Rays, MRI, CT) or just by the onset of the patient’s pain, when the problem is in an advanced status. Instead, by equipping the prosthesis with a local sensor (for the temperature as a first) and with a wireless communication radio, an early-time identification of the infection could be achieved. This paper proposes a method to transform an orthopedic device provided with holes (like a bone fixation plate) into an harvesting antenna integrating an RFID sensor, with no battery onboard. A miniaturized antenna adapter, fully embedded into a free hole, with tuning capability, collects the electromagnetic power intercepted by the medical device and transfers it to the RFID circuit. Simulations and experimentations with several prototypes demonstrated that the augmented implanted device can establish a stable RFID link up to 0.5 m and that it is able to correctly sample the variation ($37^{\circ}\text{C} - 40^{\circ}\text{C}$) of the local temperature of the bone as in case of typical deep infections.

Index Terms—Implantable Antenna, Infection Detection, Radio Frequency Identification, Smart Orthopedic Implants, Wireless Power Transfer.

I. INTRODUCTION¹

The implantation of any orthopedic devices in the body, such as prostheses or even bone fixtures, is often correlated to the risk of infection. In severe cases, the occurrence of a microbial attack can produce gradual loosening with dislocation instability and pain for the patient. In the USA, for instance, the average infection rate, including all fracture types and fixation techniques as well as prostheses, is 5 % per year [1]. Even though implants are made of biocompatible materials, they are nevertheless extraneous objects for the human body and could host pathogenic bacteria like Gram-positive cocci. Bacteria can make a colony on the surface of the implant that can advance through several stages into a *biofilm*. This one acts as a barrier with a high resistance against the immune system of the host and against traditional antibiotics [2], a thousand times higher than in case of isolated bacteria. At this stage, the only viable solution is the removal of the implant by means of surgery. An early identification of rising infection precursors could instead improve the effectiveness of antibiotics and it could moreover reduce the required dose thus avoiding more extreme countermeasures.

¹Authors are with the Pervasive Electromagnetics lab, University of Roma Tor Vergata, www.pervasive.ing.uniroma2.it. Corresponding author: gaetano.marrocco@uniroma2.it

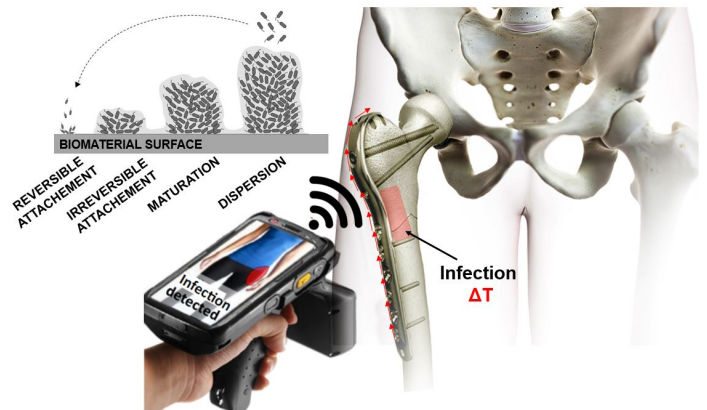


Figure 1. Concept of a remote interrogation of an RFID-based smart prosthesis to identify inflammation due to bacterial proliferation that overall produces a local temperature increase.

The current methods for the diagnose of implant-associated infections are typically indirect since they involve the measurement of some physiological and histopathological parameters by means of X-rays and Magnetic Resonance Imaging [3]. However, plain radiography suffers from low sensitivity with limited specificity. The overall accuracy of radionuclide bone imaging in the evaluation of the painful prosthetic joint was about 50-70%. This outcome is too low for clinical diagnostic use, except for qualitative screening, or in conjunction with other radionuclide markers. The C-reactive protein test (CRP) is another common procedure to detect infections with an 85% accuracy [4]. However, false positives often occur with patients previously treated with antimicrobial agents. Another indirect and non-invasive diagnostic technique is based on the temperature measurement. Tests on a large set of patients with implanted knee prosthesis [5] revealed an average temperature increase of 1.9°C (from 36.9°C to 38.8°C) in infected knee prosthesis with respect to healthy ones. Thermographic imaging of the skin surface has been already applied just above the prosthesis or on surgery wounds [6], [7]. However, the temperature gradient measured on the skin is smoothed by the thermoregulation of the human body and hence the first stage of the infection could be undetectable. More selective diagnostic procedure are based on the integration into the prosthesis itself [8] of sensors made by conducting polymers, carbon polymer composites, metal oxide semiconductors, metal organic frameworks, hydrogels, and synthetic oligomers. Other local novel techniques involve non-contacting set-up with a pH sensitive film in conjunction with the ECT (Electrical

Capacitance Tomography) [9] and a luminescent pH sensor film for monitoring bacterial growth through tissue [10].

Independently on which kind of sensor is integrated in the prosthesis, a through-the-body wireless communication link needs to be established to collect the data from the outside. Hence, the implanted prosthesis must host an integrated antenna and the required electronics. In [11], a cavity backed antenna was incorporated into a hip implant for self-monitoring at 2.4 GHz. In [12], an active wireless monitoring system at 400 MHz was integrated inside the femoral head of the hip prosthesis, with the purpose to help surgeons identifying the accurate position of the implants. In [13], flexible-substrate bio-microelectromechanical (fsBioMEMS) sensors were spread-out along the length of the fracture fixation of an ovine tibia to monitor bone fractures. Furthermore, recent progress in advanced bioresorbable/biodegradable, water-soluble materials can be exploited as well to make above implanted sensors *wrapping* and *transient* [14]. Namely they could envelope the organ to monitor and degrade over time in a predefined programmable manner based on material properties and physiological processes. An implantable stretchable and biodegradable sensor film was proposed in [15] for the independent measurement of strain and pressure following tendon and ligament surgery, as a mean of monitoring the biomechanical properties of the repair site. The bioresorbable wireless LC resonator in [16] exploits a pressure sensor acting as variable capacitor. The device could properly work up to 8 h in solution before the chemical degradation affects its function.



Figure 2. Examples of orthopedic bone-plate fixation steel plates equipped with holes for screws.

In this scenario, Radio Frequency Identification (RFID) technology can play a key role in the development and implementation of *zero-power* sensorized prostheses as it permits to avoid onboard batteries, to miniaturize the sensor and minimize the required electronics. In [17], An RFID-based telemetry system, operating at 4 kHz and 125 kHz was integrated into an hip prosthesis to measure its temperature and vibrations. The antennas of the sensor and of the interrogator are all coils. In [18], a non-radiative transcutaneous link was established at 13.56 MHz by using the RFID protocol in the HF band. Other experiments considered instead the UHF (860-960 MHz) RFID band in case of both contacting and non-contacting interrogators. In particular, a transcutaneous telemetry system, based on the near-field interaction [19]

at UHF, relies on a dipole-like antenna, equipped with a microchip and a temperature sensor, that was directly attached onto the prosthesis. In [20], a loop-transponder was integrated on the surface of the prosthesis and a non-contacting planar-F stacked antenna was used for remote interrogation up to 45 cm.

In any kind of integration, the implant must preserve the surface integrity not to hinder the insertion and not to produce inflammation by itself. Accordingly, protruding sensors must be avoided. In recently proposed integration techniques, denoted as *antennification* [21], [20], a properly modified prosthesis contributes to harvest energy by itself from the outside and to convey it to the onboard RFID integrated circuit (IC) for activation and backscattering modulation. However, those configurations require a structural modification of the prosthesis, with a not negligible impact on the re-qualification of the devices, after the change.

In this contribution, by focusing on the class of orthopedic implanted device provided with holes, like the *bone-plate fixtures* (Fig. 2), a new way to transform the object into an RFID antenna without any mechanical change of the object itself is presented. The leading idea is to plug a miniaturized field harvester, in the form of a small disk, into one of the unused screw holes of the plate so that it will collect the electric current induced onto the plate by the interrogating external field and deliver the harvested power to the RFID IC. This approach is different from all the IC/prosthesis integrations presented so far as it can be considered an addition to an existing bone-plate device, making its certification much simpler. On transforming a metal object into an efficient antenna, the key point is the impedance tuning to the RFID ICs. The proposed *antennification* method provides some degrees of freedom to control the resonant frequency and does not require a change of the external size of the harvester.

The paper is organized as follows. Section II introduces the electromagnetic rationale and the layout of the harvester. The parametric analysis and the achievable performance are resumed in Section III. Section IV describes the manufacturing of prototypes, the experimental mockup and a preliminary test with a planar body phantom. Section V shows several tests with a more realistic limb phantom employing a cow bone to determine the achievable read distance in case of identification only and of the combined identification and temperature sensing. Finally, an example of the measurement of some temperature profiles close to the bone in controlled conditions is given in Section VI.

II. RATIONALE AND HARVESTER LAYOUT

Bone-plates are like internal splints that hold the broken pieces of bone together. They are made of materials such as stainless steel and titanium. Plates can be used in several different ways and they come in various sizes and shapes to conform the affected bone where they are attached with screws (Fig. 2). The plate is hence provided with several holes for the insertion of metal screws that are only partially used. The diameter varies according to the application, to the fractured bone area and to the manufacturer. In particular, holes used

for the insertion of locking screws span from 5 to 7.3 mm [22]. Instead, holes hosting fixing screw are larger, spanning between 13 to 14 mm [23]. The *antennification* problem consists in transforming this device into an antenna, namely a dipole, that intercepts the electromagnetic field coming from the reader and transfers the collected power to the RFID IC. This job is accomplished by an antenna adapter (hereafter the *harvester*) that, without the need to break the plate, will transform one of the holes into a voltage gap avoiding protruding objects. Its input admittance $Y_A = B_A + jX_A$ must be matched to the IC admittance $Y_{IC} = G_{IC} + jB_{IC}$ so that the power transfer coefficient τ , i.e. the fraction of the RF power that is harvested by the plate and then transferred to the IC, defined [24] as :

$$\tau = 4 \frac{G_{IC} G_A}{|Y_{IC} + Y_A|^2} \leq 1 \quad (1)$$

is maximized. Denoting with G the radiation gain of the antennified prosthesis, and assuming a free-space link with the reader, the power delivered to the IC ($P_{R \rightarrow IC}$) can be expressed by the Friis formula [25]:

$$P_{R \rightarrow IC} = EIRP \left(\frac{\lambda_0}{4\pi R} \right)^2 G(\theta, \phi) \tau \eta_p \quad (2)$$

where λ_0 is the free-space wavelength, η_p is the polarization loss factor between the reader's antenna and the antennified plate, $EIRP = P_{in} G$ is the effective isotropic radiated power emitted by the reader and R is the distance between the reader and the plate.

Without any loss of generality, the antennification design method will be hereafter referred to a linear steel plate (width $W = 30$ mm, length $L = 180$ mm and thickness $P = 4$ mm) and hole radius of 7 mm.

The selected band is RFID-UHF 860-960 MHz. The adoption of RFID UHF band for prosthesis interaction offers some advantage over the LH and HF options, mostly made by multi-turn coil.

1) Despite the UHF communication is more suffering from the tissue losses than HF links, the interrogation read ranges of UHF implants proved to be much longer and suitable to collect the biophysical status of the prosthesis while the patient passes through an electromagnetic gate. Hence, there could be a remarkable application to the framework of Internet Of Things and smart-home environments [26].

2) There is a much higher flexibility in the design of the antenna that can be tailored to the specific shape of the prosthesis. The same holds for the interrogator antenna, especially when it needs to be attached on the skin [27] for long-term monitoring in mobility, thus avoiding bulky and uncomfortable coil probes as in [28].

3) There is a much wider availability in UHF than in HF bands of off-the-shelf sensor-oriented microchip transponders and readers.

4) UHF RFID arrangement may be naturally exploited as permittivity sensors too for a qualitative detection of tissue changes close to the prosthesis [29].

A. Harvester Layout

The UHF harvester module (Fig.3), to be inserted in the plate's hole comprises a metallic elliptical portion with a major axis e equal to the hole radius while the minor axis q will be adjusted for the impedance tuning (geometrical parameters in the Table I). A vertical slot in the center of the elliptical geometry hosts the voltage gap. Two curved notches, orthogonal to the previous one, will be instead used as tuning stubs that provide an inductive susceptance to balance the equivalent IC capacitance. Furthermore, two strips will house the RFID IC. The exciter is parametrized by considering two concentric ellipses with inter-ellipses distance d . The parameters controlling the admittance are hence the minor axis q of the external ellipse, stub width d and the angular size α of the notches. The harvester is placed inside a hole at a depth $t = 1$ mm from the external surface of the plate so that the points A e B (Fig.3) will be electrically in touch with the hole boundaries. The hole is then filled with two high-permittivity dielectric disks (Preperm $\epsilon_r = 12$, $\tan\delta = 0.001$ [30] and thickness $t = 1$ mm and $g = 3$ mm, respectively). In this way the surface of the fixation plate is uniform with no protruding parts.

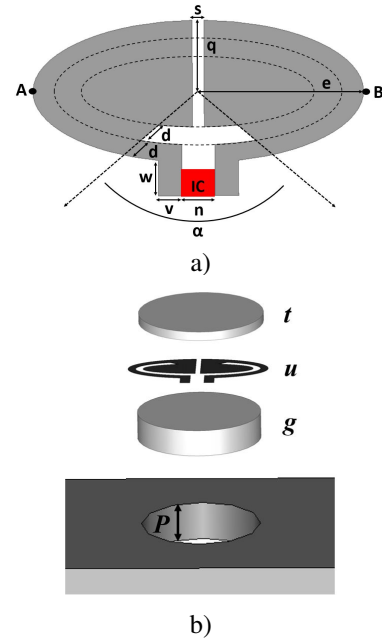


Figure 3. a) Layout of the disk harvester and relevant geometrical parameters; b) integration in hole of a plate and lower and upper insulation by means of high-permittivity covers.

Table I
ANTENNA DESIGN FIXED PARAMETERS

| Symbol | Value | Symbol | Value |
|--------|----------|--------|--------|
| t | 1 mm | e | 7 mm |
| g | 3 mm | s | 0.5 mm |
| P | 4 mm | w | 2 mm |
| r | 7 mm | v | 1 mm |
| q | 3 mm | n | 1.4 mm |
| u | 0.035 mm | | |

To make the fabrication of the prototypes easier, the hole diameter is hence set to the upper bound $2e = 14$ mm. Smaller harvesters can be designed as well by acting on the geometrical tuning parameters, and in particular on the size of the radial slot.

The reference RFID microchip is a typical temperature-sensing IC (Axzon Magnus S3 [31]) with range -40 °C < T < 85 °C and resolution 0.13 °C. This IC has already been applied for the human body measurements [32], [33], [34], [35]. Measurements in a climate chamber, where conditions can be carefully controlled, returned a precision of less than 0.2 °C and an average accuracy of less than 0.2 °C with respect to a calibrated k-type thermocouple probe sampled by a 16 bit acquisition device (MONODAQ-U-X, by DEWESoft). In the tests with the real human skin, the estimated maximum error vs. thermocouple was always less than 0.3 °C that should be enough to detect a local temperature increase due to inflammation since it produces a temperature gradient up to 1.9 °C.

Thus IC is moreover provided with self-tuning capability. Namely, it dynamically modifies his internal susceptance to compensate for possible mismatch with the antenna [24] due to variable boundary conditions. In the electromagnetic design, the chip is assumed to be in the intermediate state of the susceptance so that the analysis and experimentation will be referred to fixed RF impedance $Z_{IC} = 2.81 - j76.3\Omega$, and power sensitivity $P_{chip} = -16.6$ dBm for identification and $P_{IC} = -13.6$ dBm for sensing. This rough model will permit to derive methodological results that are also valid for other sensor-oriented ICs with static impedance such as the EM-4325 [36], the AMS-SL900 [37], the Farsens ROCKY-100 [38] and the more recently issued Asygn AS321X [39]. Nevertheless, the effect of the self-tuning against the frequency variation will be fully accounted in the next experimental Sections.

III. PARAMETRIC ANALYSIS

The achievable control on the power transfer to the IC is evaluated by a parametric analysis involving a simplified reference body model comprising a 200×200 mm planar layering (Fig.4) with geometrical size (derived from [40]) in Table II. By avoiding curved profiles, this model permits to speed-up the parametric analysis presented next. A better anthropomorphic phantom will be introduced next for a more realistic check of the achievable performance.

Table II
DIELECTRIC PARAMETERS OF THE PHANTOM

| | Skin | Fat | Muscle | Bone |
|--------------|------|-------|--------|-------|
| ϵ_r | 55 | 5.46 | 55 | 12.9 |
| $\tan\delta$ | 0.34 | 0.18 | 0.34 | 0.22 |
| H_ξ | 1 mm | 10 mm | 40 mm | 40 mm |

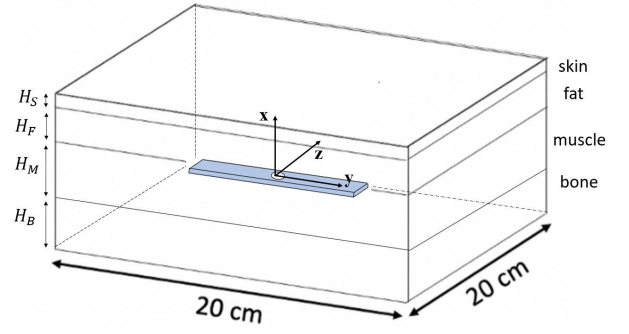


Figure 4. Planar layered model of the body for numerical simulations of the electromagnetic performance of the antennified plate.

The geometry was modeled by CST Microwave Studio and the tuning parameters investigated in the ranges: $0.25 \leq d \leq 1$ mm $3 \leq q \leq 5$ mm and $50^\circ < \alpha < 250^\circ$. Fig.5 shows the frequency profiles of τ for variation of a parameter at once when the others are fixed. It is worth showing that the proposed layout provides a two-level, coarse and fine, tuning of the peak frequency. By changing either the width d of the elliptical notches or the minor axis q , a coarse shift of the resonance frequency (60 MHz/mm for d and 30 MHz/mm for q) is produced, while by adjusting the angle α , a fine tuning of the resonance is possible (1 MHz/degree) in a very large range of frequency. Overall, by increasing d or q , a shift in the resonant frequency towards higher frequencies is produced. Instead, by increasing the angle value α , resonant frequency moves towards lower frequencies. This property can be exploited to match the tag for the specific arrangement and make the antenna working in both EU and NA bands. A better explanation of the underlying physics will be given at the end of Section III by the help of numerical simulations.

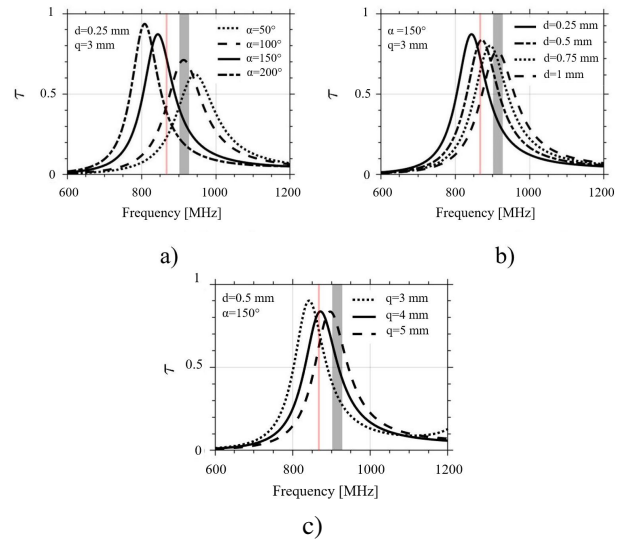


Figure 5. Parametric exploration of simulated power transmission coefficient for some value of the slot parameter a) α , having fixed $d = 0.25$ mm and $q = 3$ mm; b) of the parameter d having fixed $\alpha = 150^\circ$ and $q = 3$ mm, and c) of the parameter q , having fixed $\alpha = 150^\circ$ and $d = 0.5$ mm. Red and grey shadowed regions indicate the EU-band (865-870 MHz) and the NA-band (902-928 MHz), respectively.

Fig.6 shows a matching chart at 868 MHz, e.g. the isolines of the power transfer coefficient of the device vs. parameters $\{d, \alpha\}$ for three values of the minor axis $q = \{3, 4, 5\}$ mm. The useful regions (in gray) are those with $\tau \geq 0.8$. Noticeable, the case with $q = 3$ mm return the largest matched region so that the device will be greatly tolerant to the manufacturing imperfections.

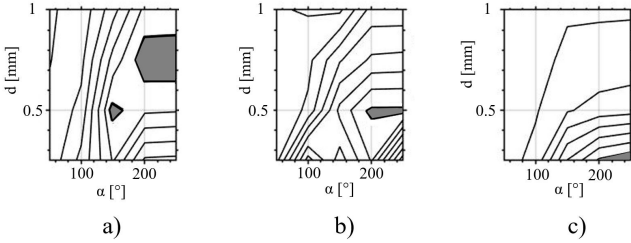


Figure 6. Isolines of the power transfer coefficients τ at 868 MHz vs. the form factor (α, d) for three values of the minor axis a) $q = 3$ mm, b) $q = 4$ mm, c) $q = 5$ mm of the external ellipse. Shaded regions indicate ranges of parameters yielding $\tau \geq 0.8$. Isoline steps: 0.1.

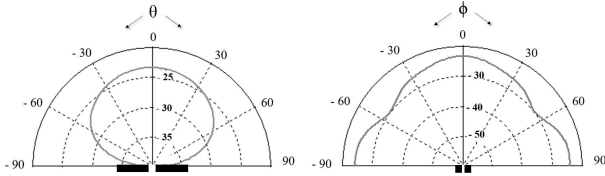


Figure 7. Horizontal and vertical cuts of the radiation gain at 868 MHz of the antennified plate.

Focusing on an harvester configuration having $q = 3$ mm, $d = 0.75$ mm and $\alpha = 200^\circ$, the horizontal and vertical cuts of the radiation gain are reported in Fig.7. The maximum value $G_{max} = -23$ dBi occurs along the normal axis of the plate and is comparable with that of other implanted UHF antennas investigated so far [20], [21]. By assuming a free-space propagation, the expected maximum read range is derived by inverting the Friis equation with the condition $P_{R \rightarrow IC} = p_{IC}$. In this case, by assuming the reader emits 3.2 W EIRP and an interrogating antenna with a circular polarization, the maximum read distance for the identification in the broadside direction will be 0.5 m in the line of sight.

The surface current density on the plate is shown in Fig.8.a. A standing wave is clearly visible. Due to the high loss of the muscle layer, the oscillations of the current quickly dump and, accordingly, there is an *active region* for radiation that is concentrated close to the hole. The overall radiating effect is that of a 35 mm implanted flat dipole. Accordingly, multiple harvesters could be embedded in the plate for multi-point sampling of the bone. For instance, Fig.8.b shows the surface current density on the plate equipped with three disk harvesters with 35 mm inter-hole distances. A comparison among the performance of the single and multiple harvesters will be given in the experimental section.

A closer inspection of the current onto the harvester (Fig.8c) permits to gain further insight in the physical behavior. The current density is mostly concentrated around the azimuthal notches that are hence the most effective tuning element, as also shown in the numerical simulation (Fig.5). The equivalent inductance L_H of each azimuthal notch increases with the angular parameter α . The current is also high around the central gap of the harvester, working as a capacitance C_H whose value is controlled by the parameter d , so that when it increases, the capacitor's arms, and accordingly the capacitance itself, reduce. By neglecting the contribute of the plate, the frequency behavior of the device, including the IC, can be roughly described as a parallel circuit as in Fig.8d so that the resonance frequency (corresponding to the peak of the power transfer coefficient), is qualitatively proportional to $1/\sqrt{2L_H(\alpha)(C_{IC} + C_H(d))}$. Accordingly, the resonant frequency moves to the left if α increases (L_H increases) or when d reduces (C_H increases), while moves to the right in the complementary cases.

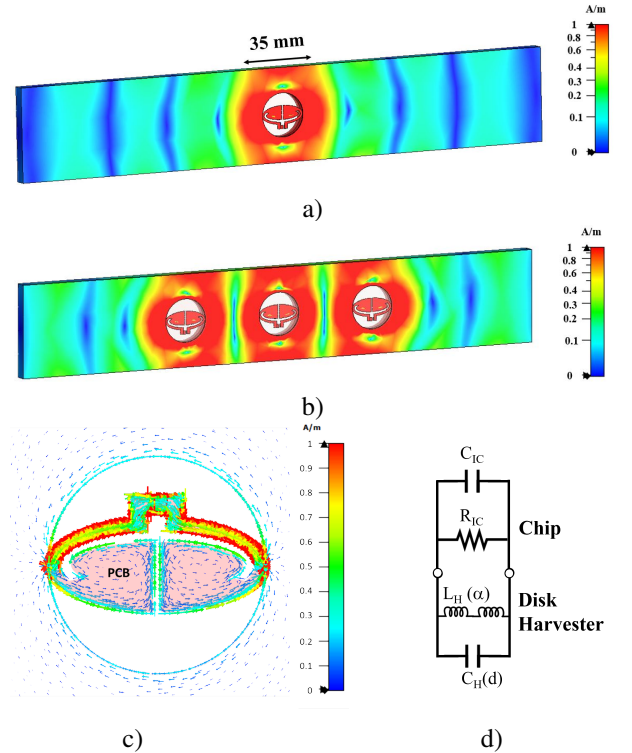


Figure 8. Simulated current density (normalized to the maximum value) at 868 MHz for the case of a) a single harvester w b) three harvesters at a mutual distance of 35 mm. c) Magnified current lines in the harvester region; d) qualitative equivalent circuit of the IC and harvester.

IV. PROTOTYPE

A. Fabrication

A mockup of the orthopedic femoral plate is made by a steel plate with the same size as in the simulations. The hole (radius $r = 7$ mm) was drilled in the middle. The disk harvester was fabricated with a milling machine on a FR4 substrate having thickness $f = 1.6$ mm Fig.9a). The microchip transponder was mounted on the strips of the harvester by a

pick and place machine and solder paste. As hot soldering is not straightforward on steel, the galvanic connection between the points A and B of the harvester and the hole boundaries was guaranteed by epoxy conductive glue (Fig.9b). A more feasible implementation, suitable for a true plug and play insertion of the hole, would deserve a specific focus that is outside the scope of this paper. Anyway, a possible solution could involve a partial vertical metallization, just below the A, B points of the lower disk of thickness g so that the two resulting vertical strips will adhere to the screw hole after plugin, thus producing a self short circuit.

The two dielectric coatings consist of high-permittivity dielectric disks (Preperm $\epsilon_r = 12$, $\tan\delta = 0.001$ [30]) having thickness $t = 1$ mm and $g = 2$ mm, respectively. Given the presence of the FR4 substrate, the value of the parameter g was deliberately reduced to ensure that the plate had no protruding parts. Five disks with different form factors were fabricated to corroborate the tuning capabilities found with the numerical simulations.

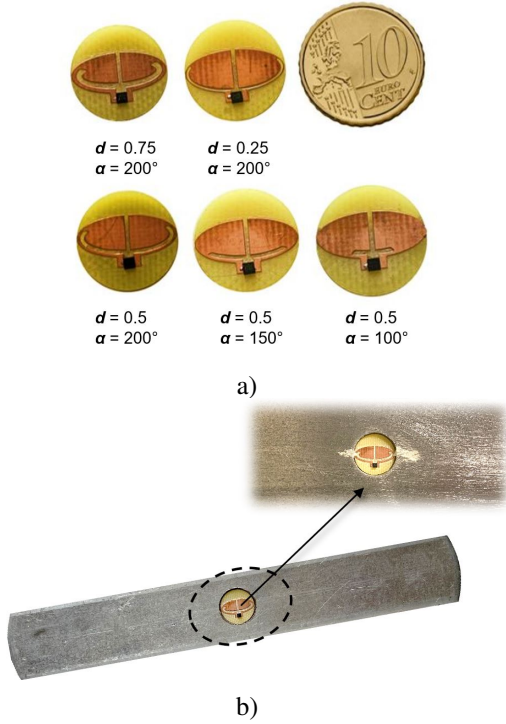


Figure 9. a) Prototypes of some harvester disks fabricated on FR-4 by etching. b) Placement of the disk inside a middle-plate hole, before covering it. Galvanic connection with the plate enforced with epoxy conductive glue.

B. Electromagnetic characterization with a planar phantom

In a first test, the body phantom was emulated by two semi-solid planar slabs of muscle and fat (Fig.10) having the same size and electromagnetic parameters as in the above electromagnetic simulation. The muscle-equivalent slab (by AET, [41]) is made by hydrogel that needs to be refurbished by water for 24 h before use.

The assembled smart implant was electromagnetically characterized in a semi-anechoic region by using the Voyantic

Tagformance station which comprises a broadband LP log-periodic antenna placed at 30 cm distance from the plate and aligned along the direction $\theta = 90^\circ$, $\phi = 0^\circ$. The performance metric is the realized gain $G \cdot \tau$, directly returned by the measurement set-up.

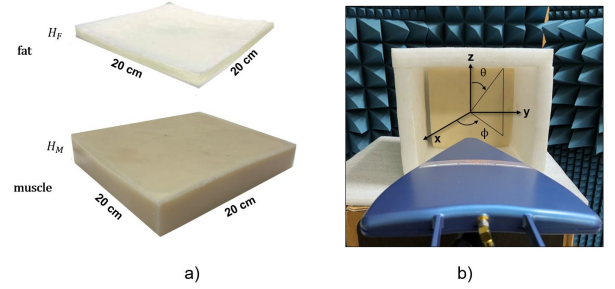


Figure 10. a) Layered phantom emulating the human body, Relative permittivity, electrical conductivity, thickness: Muscle $\epsilon_r = 54.5$, $\sigma = 0.6$ [S/m] $H_M = 4$ cm, Fat $\epsilon_r = 5.64$, $\sigma = 0.1$ [S/m] $H_F = 1$ cm. b) Measurement setup.

For a more realistic comparison with simulations, the latter also account for the self-tuning behavior of the Axzon Magnus S3 IC. Namely, as in [24], the condition $Im[Y_A(\omega) + Y_{IC}] = 0$ is enforced in the numerical evaluation of the power transfer coefficient that hence becomes :

$$\tau = 4 \frac{G_{IC} G_A}{|G_{IC} + G_A|^2}. \quad (3)$$

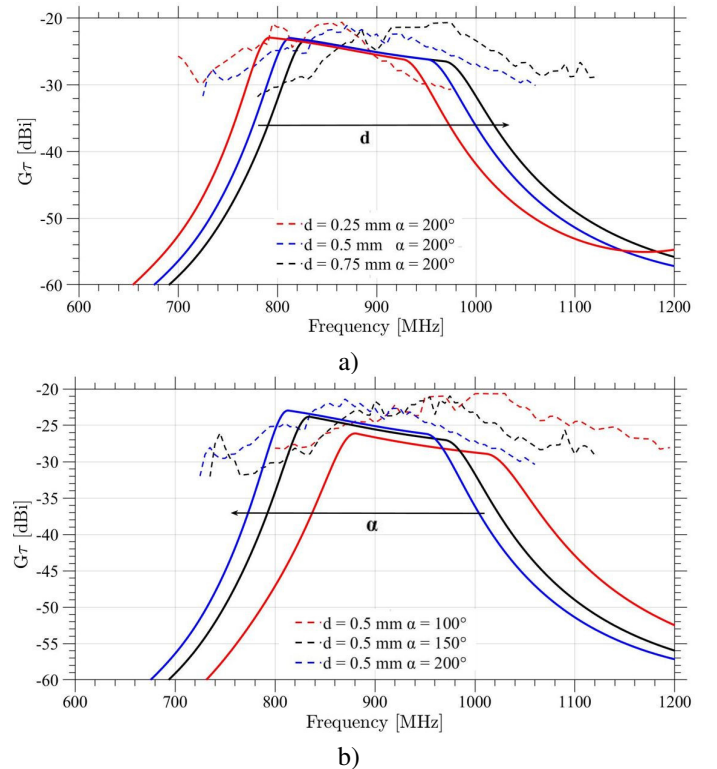


Figure 11. Layered Phantom: measured (dashed line) and simulated (solid line) realized gain $G \cdot \tau$ along the normal axis of the plate, for the five disks in Fig.9 having different values of the tuning parameters a) d and b) α . In both cases $q = 3$ mm.

Fig.11 shows the measured and simulated results versus frequency along the direction of the normal axis of the plate, for the five considered form factors of the harvester disk. The typical flat-bell profile of self-tuning ICs is clearly observed in a wide range, fully comprising the world-wide RFID band. As predicted by simulations, the measured plate response correctly shifts left or right depending on the change of the parameters d and α . Overall, the averaged peak of the realized gain in the RFID band is -22 dBi that is fully coherent with simulations.

V. TEST WITH A REAL BONE

A. Plate-bone arrangement

In a more realistic test, the plate was attached on the external surface of a cow bone (length $L = 360$ mm and diameter in the middle $D = 40$ mm). The bone was covered by the hydrogel muscle layer, wrapped around it (Fig.12).



Figure 12. a) RFID-powered fixture plate attached on the external surface of a cow bone and b) cow bone surrounded by the phantom muscle layer.

B. Measurements and comparisons

To corroborate the measurements, a corresponding numerical phantom was also simulated as a layered cylinder of bone/muscle with radius ($r_1 = 20$ mm, $r_2 = 40$ mm), respectively.

The measured and simulated realized gains of the system are reported in Fig.13. Also for this more realistic configuration, measurements are in nice agreement with simulations and the average gain among all the considered cases is still -22 dBi, as in the planar phantom. The layered model can be hence considered as a good reference configuration for the design. Fig.14 resumes the relationship between the peak frequencies of the realized gain and the tuning parameters with a relevant agreement between measurements and simulations.

The radiation pattern is analyzed in Fig.15. The pattern is broadside with a 3dB beamwidth of 148° on horizontal plane so that the interrogation is expected to be rather tolerant to possible misalignments between the reader's antenna and the implanted device. The maximum difference between measurements and simulation is just 1 dB.

Finally, the reader-tag distance was increased by 5 cm steps until the IC stopped responding. The power collected by the IC, returned by the Magnus S3 IC through the Power on

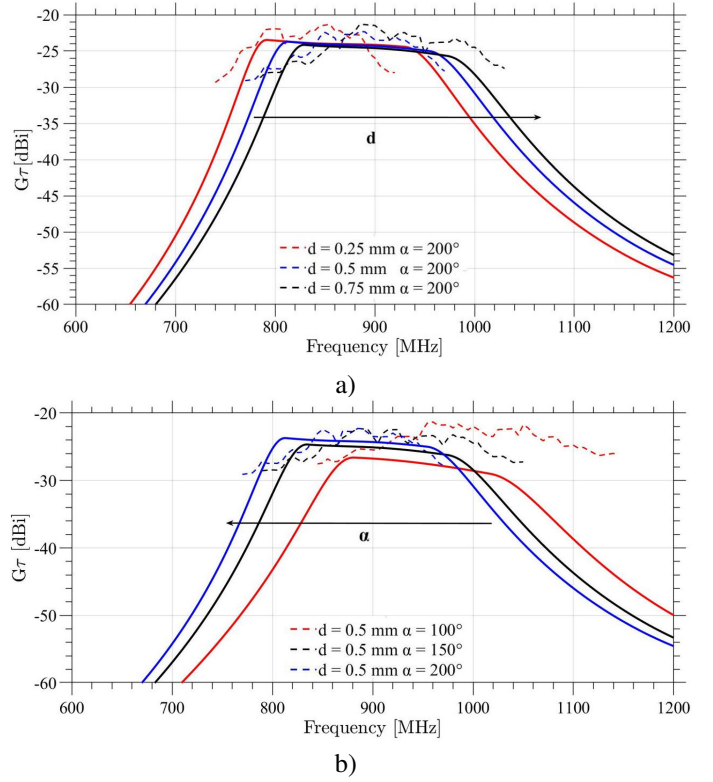


Figure 13. Bone/Cylindrical phantom: measured (dashed line) and simulated (solid line) realized gain G_r along the normal axis of the plate, for the five disks as in Fig.9 having different values of the tuning parameters a) d and b) α . $q = 3$ mm in both cases.

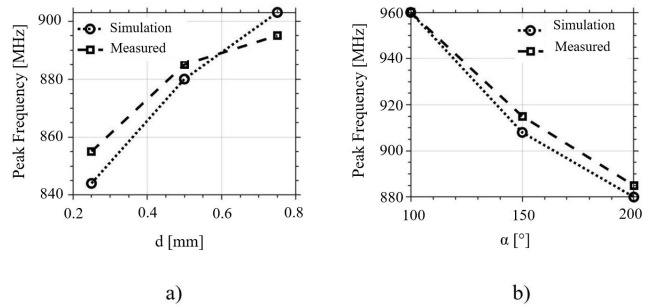


Figure 14. Bone/cylindrical phantom: simulated and measured peak frequency of realized gain vs. tuning parameters a) d and b) α .

Chip (P_{oC}) indicator, and the backscattered power (RSSI), versus the read-phantom, were collected and displayed. As the temperature measurement is reliable only when $13 \leq P_{oC} \leq 18$ [42], this indicator provides information on the maximum read distance for the temperature measurement. From Fig.16 it can be seen that, while the bone-plate can be identified up to 55 cm, the temperature will be instead reliably retrieved from a shorter, but still appreciable, distance of ~ 35 cm.

C. Multi-Sensors plate

A plate with three harvesters, as in Section III, is shown in Fig.17. The frequency profiles of the measured realized gain along the normal axis of the plate corresponding to each of

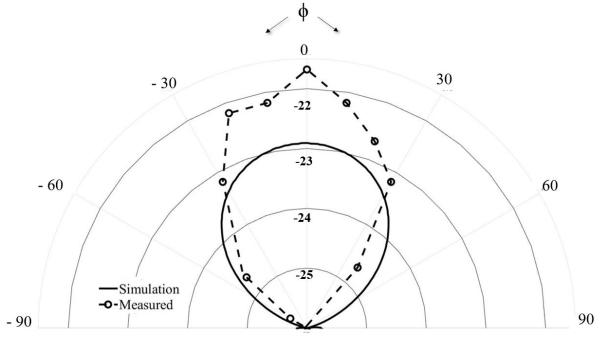


Figure 15. Bone/cylindrical phantom: measured and simulated radiation pattern $G \cdot \tau$ of the sensorized plate on the horizontal plane $\theta = 90^\circ$ of the cylindrical phantom at 868 MHz versus the azimuthal angle ϕ .

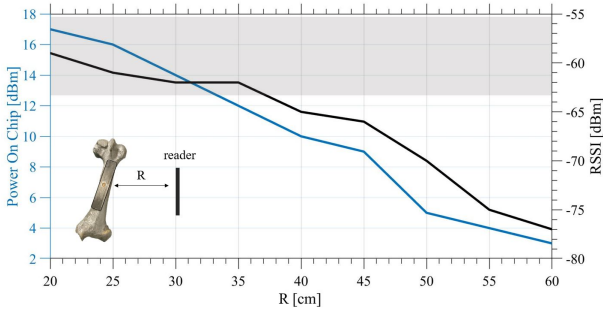


Figure 16. Measured RSSI and Power On Chip on broadside direction vs. read-phantom distance for the harvester configuration having $d = 0.5$ mm and $\alpha = 200^\circ$, $q = 3$ mm. Shaded region identifies the useful range of the Power of Chip for reliable temperature measurements.

the the three-disks show no appreciable degradation of performance w.r.t. the single-disk case confirming the potentiality to sense the temperature in several points of the plate for a better identification of the infection and for the estimation of its extension.

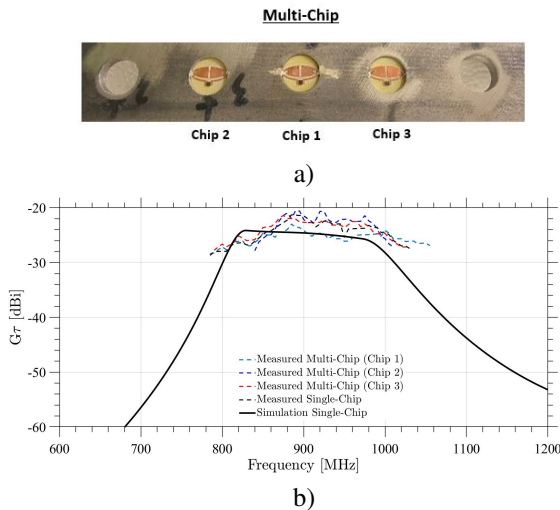


Figure 17. a) Prototype of the multi-IC plate; b) frequency-profile of the simulated realized gains $G \cdot \tau$ along the broadside direction for the Multi-Chip and Single-chip configurations.

VI. EXAMPLE OF TEMPERATURE MEASUREMENT

A realistic experiment of the measurement of the internal temperature was carried out by means of the set-up in Fig.18.

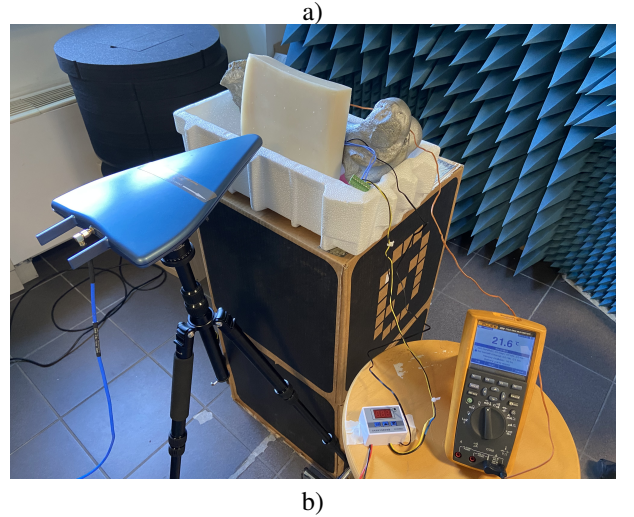
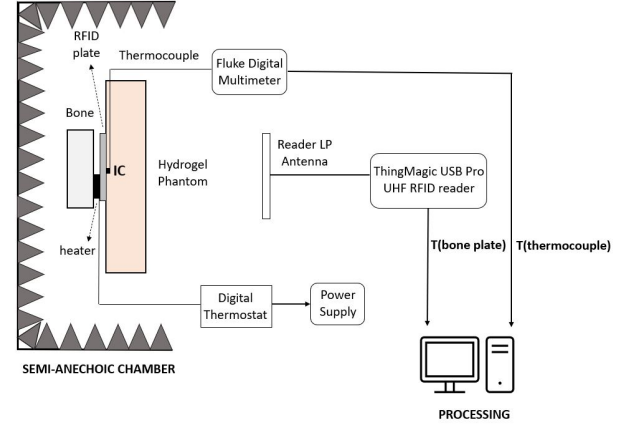


Figure 18. a) Schematic for the excitation and monitoring of a local temperature transient on the bone; b) experimental setup.

To emulate the effect of an infection, a PTC (positive temperature coefficient) heater was placed in between the antennified plate and the bone so that the IC temperature sensor will warm up through heat conduction, as in a real case. The heater was connected to a power supply and to the probe of an adjustable thermostat that permits to set two end-points temperatures $T_1 < T_2$. The power supply disconnects when the probe temperature is higher than T_2 and reconnects when it drops below T_1 . During the bone heating, the device is continuously interrogated by the reader.

Fig. 19 shows two temperature profiles. In the first one the local temperature was increased from ambient value (25°C) to the typical basal temperature of the body (37°C) in healthy conditions). Then, three cycles of warm-up and cooling-down were generated for $T_1 = 37^\circ\text{C}$ and $T_2 = 40^\circ\text{C}$ as in case of severe fever produced by a huge infections [5]). The temperature returned from the prosthesis through wireless reading is well in agreement with the wired thermocouple probe, with an average difference of 0.5°C .

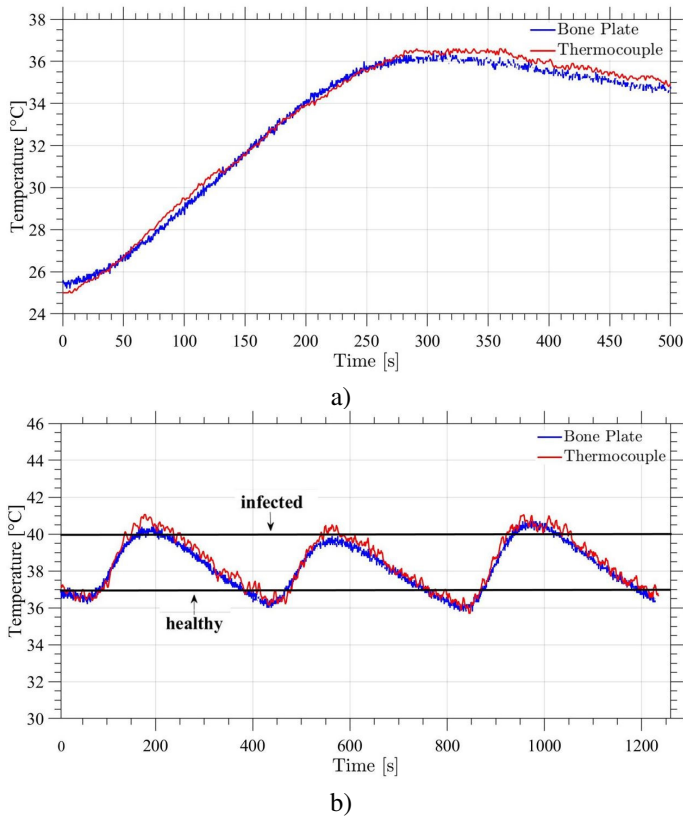


Figure 19. Temperature measurements: a) warm-up from ambient toward the basal temperature (37 °C); b) three cycles between the endpoints temperatures $T_1 = 37$ °C and $T_2 = 40$ °C (inflammation).

VII. CONCLUSION

A design method has been presented to transform a metal implanted device provided with holes into an antenna capable to work as a Radiofrequency Identification sensor. The main finding is that the proposed solution is plug-and-play and does not require any changes in the medical device thus shortening the development cycle of new products. The analysis of the active region of the surface current on the orthopedic device revealed that only a small portion of the plate is involved in the communication link. Therefore, multiple sensors could be allocated for a spatial sampling of the bone status. The antenna adapter is small in size and provides several degrees of freedom for the tuning of the working frequency. The performance as implanted antenna is comparable with the state of the art and will permit to collect the local temperature on the affected bone by using Commercial Off The Shelf (COTS) RFID readers in a non-invasive way. The resulting augmented medical device could enable a preventive identification of infections by qualified points of care and even by the user himself. Even though the idea was applied to a flat plate and to the temperature, the extension to non-planar devices is straightforward and it was already experimented by the authors.

A deeper evaluation of the proposed device, and in particular its expected capability to detect small changes of the local temperature due to infections, would deserve a more realistic phantom reproducing the thermo-regulation phenomena

related to vascularization and hydration. To this purpose, *in-vivo* tests and a clinical trial with an engineered device should be planned in future in collaboration with physicians.

Finally, further extension of the method will include the integration of other sensors, for the pH as a first, to provide complementary information for a more careful evaluation of the infection grade.

REFERENCES

- [1] T.F. Moriarty, U. Schlegel, S. Perren and R.G. Richards, "Infection in fracture fixation: can we influence infection rates through implant design", *Journal of Material Science : Materials in Medicine*, vol.21, pp.1031-1035, 2010
- [2] U. Filipovic, R.G. Dahmane, S. Ghannouchi, A. Zore and K. Bohinc, "Bacterial adhesion on orthopedic implants", *Advances in Colloid and Interface Science*, vol. 283:102228, 2020
- [3] C. Love, S.E. Marwin and C.J. Palestro, "Nuclear medicine and the infected joint replacement", *Seminars in nuclear medicine*, vol. 39, no. 1, pp. 66-78, 2009
- [4] M. Müller, L. Morawietz, O. Hasart, P. Strube, C. Perka and S. Tohtz, "Diagnosis of periprosthetic infection following total hip arthroplasty—evaluation of the diagnostic values of pre-and intraoperative parameters and the associated strategy to preoperatively select patients with a high probability of joint infection", *Journal of orthopaedic surgery and research*, vol. 3, no. 31, pp. 1-8, 2008
- [5] C. L. Romanò, R. D'Anchise, M. Calamita, G. Manzi, D. Romanò, and V. Sansone, "Value of digital telethermography for the diagnosis of septic knee prosthesis: A prospective cohort study," *BMC Musculoskeletal Disorders*, vol. 14, no. 1, p. 7, 2013
- [6] C. L. Romanò, D. Romanò, F. Dell'Oro, N. Logoluso and L. Drago, "Healing of surgical site after total hip and knee replacements show similar telethermographic patterns", *J. Orthopaedics Traumatol.*, vol. 12, no. 2, pp. 81-86, 2011
- [7] J. Christensen, L. H. Matzen, M. Vaeth, S. Schou and A. Wenzel, "Thermography as a quantitative imaging method for assessing postoperative inflammation", *Dentomaxillofacial Radiol.*, vol. 41, no. 6, pp. 494-499, 2012
- [8] H. Devaraj, K.C. Aw and A.J. McDaid, "Review of functional materials for potential use as wearable infection sensors in limb prostheses", *Biomedical engineering letters*, vol. 10, no. 1, pp. 43-61, 2020
- [9] S. Gupta and K. J. Loh, "Noncontact Electrical Permittivity Mapping and pH-Sensitive Films for Osseointegrated Prosthesis and Infection Monitoring", *IEEE Transactions on Medical Imaging*, vol. 36, no. 11, pp. 2193-2203, 2017
- [10] F. Wang Y. Raval, H. Chen, T.J. Tzeng, J.D. DesJardins and J.N. Anker, "Development of luminescent pH sensor films for monitoring bacterial growth through tissue", *Advanced healthcare materials*, vol. 3, no. 2, pp. 197-204, 2014
- [11] E. Cil and S. Dumanli, "Characterization of an implanted antenna inside a 3D printed multilayer hip phantom", *13th European Conference on Antennas and Propagation (EuCAP)*, pp. 1-4, Krakow, Poland, 2019
- [12] H. Chen, J. Gao, S. Su, X. Zhang and Z. Wang, "A Visual-Aided Wireless Monitoring System Design for Total Hip Replacement Surgery," *IEEE Transactions on Biomedical Circuits and Systems*, vol. 9, no. 2, pp. 227- 236, 2015
- [13] J.G. Wolynski, C.J. Sutherland, H.V. Demir, E. Unal, A. Alipour, C.M. Puttlitz and K.C. McGilvray, "Utilizing multiple bioMEMS sensors to monitor orthopaedic strain and predict bone fracture healing", *Journal of Orthopaedic Research*, vol. 37, no. 9, pp. 1873-1880, 2019
- [14] C Pang, C Lee, KY Suh, "Recent advances in flexible sensors for wearable and implantable devices", *J. Appl. Polym. Sci.*, Wiley online library, pp. 1429-1441, 2013
- [15] C.M. Boutry, Y. Kaizawa, B.C. Schroeder, A. Chortos, A. Legrand, Z. Wang, J. Chang, P. Fox, Z. Bao, "A stretchable and biodegradable strain and pressure sensor for orthopaedic application", *Nature Electronics*, vol.1, pp. 314-321, 2018
- [16] A. Palmroth, T. Salpavaara, J. Lekkala, M. Kellomaki, "Fabrication and characterization of a wireless Bioresorbable pressure sensor", *Advanced Materials Technology*, vol.4, no. 9, pp. 1900428, 2019
- [17] U. Marschner et al., "Integration of a wireless lock-in measurement of hip prosthesis vibrations for loosening detection" *Sens. Actuators A, Phys.*, vol. 156, no. 1, pp. 145-154, 2009

- [18] X. Liu, J. L. Berger, A. Ogirala, and M. H. Mickle, "A touch probe method of operating an implantable RFID tag for orthopedic implant identification," *IEEE Trans. Biomed. Circuits Syst.*, vol. 7, no. 3, pp. 236–242, Jun. 2013
- [19] X. Liu, J. R. Stachel, E. Stachel, M. H. Mickle, and J. L. Berger, "The UHF Gen 2 RFID system for transcutaneous operation for orthopedic implants," in *Proc. IEEE Int. Instrum. Meas. Technol. Conf. (I2MTC)*, pp. 1620–1623, May 2013,
- [20] R. Lodato and G. Marrocco, "Close Integration of a UHF-RFID Transponder Into a Limb Prosthesis for Tracking and Sensing", in *IEEE Sensors Journal*, vol. 16, no. 6, pp. 1806-1813, March15, 2016
- [21] S. Nappi, L. Gargale, P.P. Valentini, G. Marrocco, "RF detection of micro-cracks in orthopedic implants by conformal space filling curves", in *2019 IEEE International Conference on RFID Technology and Applications (RFID-TA)*, pp. 240–243, 2019.
- [22] <http://synthes.vo.llnwd.net/o16/Mobile/Synthes%20International/KYO/Trauma/PDFs/056.000.403.pdf>
- [23] http://synthes.vo.llnwd.net/o16/LLNWMB8/INT%20Mobile/Synthes%20International/Product%20Support%20Material/legacy_Synthes_PDF/DSEM-TRM-1114-0221-4d_LR.pdf
- [24] M. C. Caccami and G. Marrocco, "Electromagnetic modeling of self-tuning RFID sensor antennas in linear and nonlinear regimes," *IEEE Trans. Antennas Propag.*, vol. 66, no. 6, pp. 2779-2787, June 2018
- [25] C. A. Balanis, *Antenna Theory: Analysis and Design, 4th Edition*. John Wiley & Sons, 2016.
- [26] S. Amendola, R. Lodato, S. Manzari, C. Occhiuzzi, and G. Marrocco, "RFID technology for IoT-based personal healthcare in smart spaces," *IEEE J. Internet Things*, vol. 1, no. 2, pp. 144–152, Apr. 2014
- [27] C. Miozzi, G. Saggio, E. Gruppioni and G. Marrocco, "Constrained Safety-Integrity Performance of Through-the-Arms UHF-RFID Transcutaneous Wireless Communication for the Control of Prostheses," in *IEEE Journal of Radio Frequency Identification*, vol. 3, no. 4, pp. 236-244, Dec. 2019
- [28] G. Bergmann, F. Graichen, J. Dymke, A. Rohlmann, G. N. Duda, and P. Damm, "High-tech hip implant for wireless temperature measurements in vivo," *PLoS One*, vol. 7, no. 8, pp. 1–7, 2012
- [29] C. Occhiuzzi, G. Contri, and G. Marrocco, "Design of implanted RFID tags for passive sensing of human body: The STENTag," *IEEE Trans. Antennas Propag.*, vol. 60, no. 7, pp. 3146–3154, Jul. 2012
- [30] PPE1200, Preperm. [Online]. Available: <https://www.preperm.com/products/raw-materials/#preperm-standardgrades>
- [31] Magnus S3, Axzon. [Online]. Available: <https://axzon.com/rfm3300-dmagnus-s3-m3d-passive-sensor-ic/>
- [32] G. M. Bianco and G. Marrocco, "Sensorized Facemask With Moisture-Sensitive RFID Antenna", in *IEEE Sensors Letters*, vol. 5, no. 3, pp. 1-4, Art no. 6000604, March 2021
- [33] C. Miozzi, F. Amato and G. Marrocco, "Performance and Durability of Thread Antennas as Stretchable Epidermal UHF RFID Tags", in *IEEE Journal of Radio Frequency Identification*, vol. 4, no. 4, pp. 398-405, Dec. 2020
- [34] F. Camera, C. Miozzi, F. Amato, C. Occhiuzzi and G. Marrocco, "Experimental Assessment of Wireless Monitoring of Axilla Temperature by Means of Epidermal Battery-Less RFID Sensors", in *IEEE Sensors Letters*, vol. 4, no. 11, pp. 1-4, Art no. 6002304, Nov. 2020
- [35] F. Camera and G. Marrocco, "Electromagnetic-Based Correction of Bio-Integrated RFID Sensors for Reliable Skin Temperature Monitoring," *IEEE Sensors Journal*, vol. 21, no. 1, pp. 421-429, 1 Jan.1, 2021
- [36] EM-4325. [Online]. Available: https://www.emmicroelectronic.com/sites/default/files/products/datasheets/4325-ds_0.pdf
- [37] AMS SL900A. [Online]. Available: https://ams.com/documents/20143/36005/SL900A_DS000294_5-00.pdf/d399f354-b0b6-146f-6e98-b124826bd737
- [38] Farsens. [Online]. Available: <http://www.farsens.com/wp-content/uploads/2017/12/DS-ROCKY100-V04.pdf>
- [39] Asygn. [Online]. Available: <https://asygn.com/as321x/>
- [40] Dielectric Properties of Body Tissues, IFAC. [Online] Available: <http://niremf.ifac.cnr.it/tissprop/htmlclie/htmlclie.php>
- [41] "Human body equivalent phantom in low-frequency, microwave, and millimeter-waves, <https://www.aetassociates.com/pdf/electromagnetic.pdf>"
- [42] Application Note AN006 Sensor And Temperature Measurements.